

1 **Subtracting tilt from a horizontal-seismometer using a**
2 **ground-rotation-sensor**

3
4 Krishna Venkateswara¹, Charles A. Hagedorn, Jens H. Gundlach

5 University of Washington, Seattle WA USA

6 Jeffery Kissel, Jim Warner, Hugh Radkins, Thomas Shaffer

7 LIGO Laboratory, Hanford WA USA

8 Brian Lantz

9 Stanford University, Stanford CA USA

10 Richard Mittleman, Fabrice Matichard

11 MIT, Cambridge MA USA

12 Robert Schofield

13 University of Oregon, Eugene OR USA

14 **ABSTRACT** We demonstrate the use of a high-precision ground-rotation-sensor to
15 subtract wind induced tilt noise in a horizontal broadband seismometer at frequencies above 10
16 mHz. The measurement was carried out at the LIGO Hanford Observatory using a low-frequency

¹ kvenk@uw.edu

17 flexure-beam-balance with an autocollimator readout and a T240 seismometer, located in close
18 proximity to each other. Along their common horizontal axis, the two instruments show
19 significant coherence below 100 mHz, which increases as a function of wind speed due to floor
20 tilt induced by wind pressure on the walls of the building and the ground outside. Under wind
21 speeds of 20-30 mph, correcting the seismometer for measured ground-rotation lowered the
22 signal by a factor of ~10 between 10-100 mHz. This paper describes the instruments used, shows
23 representative data for low and high wind speeds, and discusses the tilt-subtraction and possible
24 limitations.

25 INTRODUCTION

26 The inability to distinguish between time-varying horizontal displacement and slow rotation (tilt)
27 by seismometers has been a long standing problem in seismology (**Rodgers (1968)**, **Lee *et al.***
28 **(2009)**) with important ramifications in active seismic isolation (**Lantz *et al.* (2009)**). This is
29 because seismometers are essentially acceleration sensors and a horizontal acceleration sensor
30 alone is insufficient to distinguish between the two sources of acceleration - acceleration from
31 horizontal translation or that due to gravity coupling through rotation. Ordinary tiltmeters, such
32 as simple pendulums or spirit levels, also suffer from the same problem since they gauge tilt by
33 comparing horizontal acceleration to the vertical (at frequencies below their resonances).

34 In this paper, we define ‘tilt’ of the ground as its angle with respect to the horizontal axis of a
35 nearly inertial frame fixed to the local gravitational vertical (defined by a free-falling mass). This
36 frame is not strictly inertial, because of changes in local gravity and Earth's rotation. However,
37 these effects are small in the frequency region under discussion (above 10 mHz) and are ignored
38 here (see Appendix B for a brief discussion).

39 The apparent displacement as interpreted by a seismometer due to a tilt θ at angular frequency
40 $\omega = 2\pi f$ is given by

$$|x| = \frac{g}{\omega^2} |\theta| \quad (1)$$

41 Due to the ω^2 in the denominator, response to tilt can often dominate seismometer output below
42 0.1 Hz.

43 One way to separate displacement and rotation is to measure absolute tilt/rotation (i.e. with
44 respect to the inertial frame), using beam-balances (see **Robertson *et al.* (1982)**, **Speake and**
45 **Newell (1990)**) or through other means such as ring-laser-gyroscopes (see **Belfi *et al.* (2012)**).
46 This independent sensor can then be used to subtract the tilt component from a seismometer's
47 output to provide a pure displacement output. In theory, the effectiveness of subtraction
48 techniques is limited only by the noise in the two sensors. In practice, it is also limited by the
49 extent to which the tilt signal is similar for the two instruments. Mechanical filtering of the tilt
50 transmission to a seismometer is an interesting alternative technique of measuring tilt-free
51 horizontal displacement (**Matichard *et al.* (2015)**) as compared to direct tilt measurement and
52 subtraction.

53 We demonstrate tilt-subtraction using a low-frequency beam-balance whose angle is measured
54 using a high-sensitivity autocollimator. Two such rotation sensors were built at the University of
55 Washington, Seattle (UW). The main features and performance of the first sensor are
56 summarized in **Venkateswara *et al.* (2014)**. The second sensor was built and tested at UW and
57 subsequently installed at the LIGO Hanford Observatory (LHO), where tilt motion currently
58 limits the performance of the active isolation platforms at low frequency (**Matichard, Lantz *et***
59 ***al.* (2015)**). This second instrument is referred to as the Beam-Rotation-Sensor (BRS). The

60 requirement for a ground rotation sensor to improve the active seismic isolation in Advanced
61 LIGO (Aasi, J *et al.* (2015)) is described in Lantz *et al.* (2009).

62 **Discussion of other tiltmeters:** In the last three decades, several sensitive rotation-sensors
63 have been proposed or built (see Matichard and Evans (2015) for a review of the field).
64 Speake and Newell (1990) developed a tiltmeter based on a dumbbell suspended by crossed-
65 flexures near its center of mass, establishing limits of $1 \text{ nrad}/\sqrt{(\text{Hz})}$ between 3-10 Hz.
66 Winterflood *et al.* (2000) developed a tilt sensor composed of a bar suspended by a metallic
67 glass flexure with a shadow-sensor readout with a reported sensitivity of $0.2 \text{ nrad}/\sqrt{(\text{Hz})}$ above 1
68 Hz. More recently, Dergachev *et al.* (2014) developed a tilt sensor consisting of a beam-balance
69 suspended by two knife-edges and an air-core LVDT readout. They report a tilt sensitivity of 5.7
70 $\text{ nrad}/\sqrt{(\text{Hz})}$ sensitivity at 10 mHz and $0.64 \text{ nrad}/\sqrt{(\text{Hz})}$ above 0.1 Hz.

71 Vertically oriented Ring Laser Gyroscopes can also be very sensitive tiltmeters (Korth *et al.*
72 (2015), Schreiber and Wells (2013)). Belfi *et al.* (2012), report on a 1.82-m^2 ring laser gyro
73 with sensitivity of $3 \text{ nrad}/\sqrt{(\text{Hz})}$ at 0.1 Hz and better than $0.1 \text{ nrad}/\sqrt{(\text{Hz})}$ above 3 Hz.

74 **DESCRIPTION OF THE INSTRUMENTS**

75 The BRS consists of a 0.86-m beam-balance, suspended by two Beryllium-Copper flexures. Its
76 angle is measured with respect to a reference mirror using a differential autocollimator described
77 in Arp *et al.* (2014). The reference mirror is a beam-splitter mounted rigidly with respect to the
78 ground and in the same optical path as the target mirror on the beam-balance. Measurement of
79 the beam-balance angle relative to the reference mirror allows for subtraction of any common-
80 mode noise, such as thermal drift of the autocollimator body. As suspended, the resonant

81 frequency of the beam-balance is 8.79 mHz, moment of inertia of 0.59-kg-m² and the mechanical
82 quality factor is 4.8×10^3 . It is placed in a vacuum vessel which is pumped down to pressures of
83 less than 10^{-4} Pa by an ion pump.

84 A detailed discussion of the tilt and acceleration-sensitivity of a beam-balance, such as the BRS
85 is given in **Venkateswara et al. (2014)**. A schematic of the BRS with relevant angles is shown
86 in Figure 1. When the ground tilts at frequencies above the BRS resonance frequency, the
87 balance tends to stay fixed w.r.t. the inertial frame, thus the autocollimator measures the ground
88 rotation w.r.t. the inertial frame (inertial-tilt). If the center of mass of the balance is located at the
89 pivot/suspension point, then ground acceleration applies no torque on the balance. Detailed
90 discussion of the dynamics is given in Appendix A. Appendix B discusses the effect of earth's
91 rotation on the BRS.

92 The suspension frame of the beam-balance is firmly clamped to the base of a vacuum vessel,
93 which in turn was secured to a 2.5-cm thick and 0.9-m by 0.6-m aluminum plate. The three feet
94 of this plate rest on the concrete floor of the X-End-station of the LIGO Hanford Observatory.
95 The foundation is approximately 0.8-m-thick. Small rubber shims, roughly 3-mm-thick, were
96 placed under the feet of the BRS-plate to isolate it from any high-frequency vibration. The entire
97 apparatus, including the baseplate, is enclosed in a 5-cm-thick rigid-foam enclosure which
98 provides passive thermal insulation and shielding from air flows. The hall is temperature
99 controlled to roughly +/- 0.5 deg C.

100 The seismometer used for this study was a Nanometrics Trillium 240 Broadband Sensor. It was
101 located about 1 m away from the center of the BRS. It also has three feet which rest on the same
102 floor and has a separate thermal enclosure.

103 A cup anemometer (part of a Davis Weather Station-II), mounted to the roof of the End-station,
104 is used to record wind-speed and direction.

105 **DATA AT HIGH WIND-SPEEDS**

106 Figure 2 shows the amplitude spectral density (ASD) of data taken with the BRS during a windy
107 period. The data were taken for 5000 seconds on May 16 2015 from 3:20 to 4:43 UTC for the
108 ASD, which was calculated using the periodogram method and averaged over five frequency
109 bins. The wind speeds were roughly between 20 and 30 mph as shown in Figure 3.

110 The raw angular position (autocollimator output) of the BRS is labelled simply as ‘BRS angle’
111 (θ_a). The resonance of the beam-balance is visible at 8.9 mHz. The peak visible at 3.1 Hz is due
112 to the torsional mode of the balance, coupling in through small asymmetries in the angular
113 readout. Also shown is the ‘BRS ref’ signal, the angular motion of the reference mirror used in
114 the BRS autocollimator. As the autocollimator output is the difference in angle between the
115 mirror on the beam-balance and the reference mirror, BRS ref can be interpreted as $1/\sqrt{2}$ times
116 the upper limit of the angle readout noise. Any common-noise (such as thermal drifts) between
117 the two is subtracted while other noise (such as electronic noise) adds incoherently, increasing
118 the total by a factor of $\sqrt{2}$.

119 The horizontal acceleration, a_x , as measured by the T240 seismometer located close to the BRS
120 will be influenced by both horizontal displacement of the ground and ground tilt. Ideally if the
121 separation between the center of mass (COM) and the suspension point/pivot of the beam-
122 balance (‘d’) were negligibly small, then the BRS would be sensitive only to ground tilt.

123 However, due to a small but finite ‘ d ’, BRS output is also influenced by horizontal acceleration
 124 and this must be corrected in order to separate the two.

125 To convert the autocollimator measured angle of the BRS to ground tilt, we use the following
 126 equation (derived in Appendix A) in frequency space:

$$\theta_p = - \frac{\omega^2 - \omega_0^2(1 + i\varphi)}{\omega^2} \theta_a + \frac{Md}{I\omega^2} a_x \quad (2)$$

127 where θ_p is the ground tilt at angular frequency ω , ω_0 is the resonant frequency, I is the moment
 128 of inertia, M is the total mass, and d is the separation between the center of mass (COM) and the
 129 suspension point/pivot of the beam-balance, and a_x is the horizontal acceleration measured by
 130 the T240.

131 The result of the ground-tilt computation is shown in Figure 4. The first term on the right-hand-
 132 side in Eq. (2) is the inversion of the ideal beam-balance response (labelled as ‘Ground-tilt
 133 according to BRS’) and the second is an acceleration-response correction (labelled as ‘Correction
 134 using T240’) due to a small but finite ‘ d ’, separately measured to be $(33 \pm 5) \mu\text{m}$. Alternatively,
 135 ‘ d ’ could be extracted by fitting the low-frequency part of the BRS and T240 data which yields
 136 the same value of d . To show the readout-noise contribution, we also apply the first term in Eq.
 137 (2) to the BRS ref data ($\times \sqrt{2}$), labelled as ‘BRS readout noise contribution’.

138 The computed ground-tilt can then be converted into acceleration units by multiplying by the
 139 acceleration due to gravity, g , and then subtracting it from the measured acceleration as shown in
 140 Fig. (5). The plot shows the ASD of the T240 acceleration, the corrected ground-tilt contribution
 141 and the tilt-subtracted residual. The frequency response of the T240 instrument response has
 142 been compensated. The residual horizontal acceleration is smaller than the seismometer

143 amplitude between 6 to 90 mHz by factors of 2-10. The BRS noise contribution, computed as g
144 times the BRS ref noise contribution, is also shown.

145 There are several noteworthy features in Fig. (5). Although the micro-seismic amplitude was
146 relatively small during this period, it is interesting to note that even at 0.2 Hz, tilt accounts for
147 one-fifth of the horizontal acceleration measured by the seismometer. The average ground
148 rotation spectral density is relatively smooth at low frequencies but falls off quickly above ~ 0.3
149 Hz.

150 At frequencies above 0.1 Hz, the acceleration residual matches the T240 acceleration. Between
151 35 to 100 mHz, it decreases as nearly f^2 , but below 30 mHz, it goes as $1/f^2$. If the tilt-
152 subtraction were limited only by the BRS readout noise, one would expect the f^2 -trend to
153 continue until it intersects the BRS noise contribution curve and to then follow that curve. This
154 deviation indicates an excess noise contribution at low frequencies, discussed in subsequent
155 sections. Figure 6 shows a plot of the transfer function between translation measured by the
156 seismometer and the tilt measured by BRS. Also shown are two straight line fits to the data at
157 low and high frequencies. At low frequencies, the translation has the expected g/ω^2
158 dependence. At frequencies near 1 Hz, the translation appears to be proportional to the tilt,
159 indicating rotation about a pivot ~ 10 meters underground. If this relation were to hold down to
160 10 mHz, the wind-induced horizontal acceleration ASD would be $\sim 2 \text{ nm/s}^2/\sqrt{(\text{Hz})}$. This is far
161 too small to explain the excess noise in the acceleration residual.

162 The first plot in Figure 7 shows the coherence between the T240 and BRS data and between the
163 sensors and the residual acceleration. The low coherence for the latter two curves shows that the
164 subtraction removes most of the common (tilt) signal between the two instruments. The second

165 plot in Figure 7 is an estimate of the expected subtraction factor based on the observed
166 coherence, calculated as

$$sub.factor = \frac{1}{\sqrt{1 - coherence}} \quad (3)$$

167 The ratio of the T240 acceleration to the residual acceleration is shown, which agrees well with
168 the expected subtraction factor. The slight decrease in the ratio near 0.1 Hz is due to the extra
169 coherence between the two instruments caused by the direct rotation to translation coupling
170 discussed in Figure 6. As the goal is to measure the inertial translation of the ground, we do not
171 subtract this direct coupling.

172 Figure 8 shows the ASD of data taken with the BRS and a T240 seismometer during another
173 windy period. The data were taken for 5000 seconds on October 12, 2014, from 00:45 to 2:09
174 UTC and averaged five times for the ASD, as before. The wind speeds were roughly between 20
175 and 30 mph as shown in Figure 9. Also shown in Figure 8 is a second T240 acceleration
176 spectrum measured about 3 hours later when wind speeds were lower. In this case, it is
177 particularly interesting to note that the high-wind seismometer spectrum is swamped by tilt-noise
178 below 0.1 Hz and cannot resolve the primary micro-seismic peak. But after, tilt-subtraction, the
179 peak is distinct and this peak height matches with that measured 3 hours later. As the primary
180 micro-seismic peak height varies only slowly with time, this indicates that the acceleration
181 residual is indeed mainly composed of acceleration from horizontal ground displacement.

182 **DATA AT LOW WIND-SPEEDS**

183 Figure (10) shows a similar tilt-subtraction for low wind-speed data, as measured with the BRS
184 and the T240 seismometer. The data were taken for 5000 seconds on May 14, 2015 from 02:00
185 to 03:23 UTC. The wind speeds were mostly below 4 mph as shown in Figure 11.

186 In Figure 10, the measured ground tilt is limited by the BRS noise above ~ 60 mHz. Below that,
187 BRS measures a rising background which separates from the noise. The BRS noise looks nearly
188 identical to that in the previous cases indicating that the intrinsic noise of the autocollimator is
189 unchanged between the two cases. The acceleration residual is dominated by the T240
190 acceleration above 30 mHz. It is also interesting to note that the increase in ground rotation is
191 nearly a factor of 100 in the 20-100 mHz range between Figure 5 and Figure 10, whereas the
192 average increase in wind-speed is only a factor of ~ 10 , indicating a strongly non-linear relation
193 between the two. The drag force in air is proportional to the square of the flow velocity, which
194 qualitatively agrees with the above observation.

195 **DISCUSSION OF TILT-SUBTRACTED ACCELERATION**

196 **RESIDUAL**

197 From our experiments, it is clear that ground tilt can be measured and subtracted effectively from
198 horizontal acceleration measurements. Under high-wind conditions, the tilt-subtracted residual
199 acceleration is significantly lower than the seismometer output above 10 mHz but not as low as
200 the residual under low-wind conditions, as one might expect if the same signal was being
201 measured by the two instruments. Figure 12 shows an ASD of the tilt-subtracted residuals for the

202 quiet case and the windy case along with the expected readout noise contribution. Based on
203 Figure 6 and the discussion in the previous section, it is likely not due to increase in ground
204 translation. Recent measurements made by placing a second seismometer on the floor at various
205 distances from the first seismometer show that the tilt varies substantially over the floor. This
206 suggests that the increase in the tilt residual arises from the small differences in tilt seen by the
207 BRS and the seismometer. Further improvement in subtraction could likely be achieved by
208 placing both instruments on a common platform.

209 CONCLUSION

210 Tilt-subtraction from a horizontal seismometer has been demonstrated using a ground-rotation
211 sensor located ~ 1 m away. The rotation-sensor consists of a flexure-suspended beam-balance
212 with an autocollimator readout with intrinsic sensitivity of $0.15 \text{ nrad}/\sqrt{(\text{Hz})}$ above 0.1 Hz. This
213 instrument meets the requirement for a ground rotation sensor to improve Advanced LIGO
214 described in **Lantz et al. (2009)**. A tilt-subtraction factor of 10 is achieved at 30 mHz under
215 wind-speeds of 20-30 mph.

216 DATA AND RESOURCES

217 Data used in this study were collected at the LIGO Hanford Observatory. It can be provided
218 upon request.

219 ACKNOWLEDGEMENTS

220 This work was carried out at the LIGO Hanford Observatory by members of LIGO laboratory,
221 and the LIGO Scientific Council including University of Washington, Seattle, Stanford

222 University and University of Oregon. LIGO was constructed by the California Institute of
223 Technology and Massachusetts Institute of Technology with funding from the National Science
224 Foundation (NSF), and operates under cooperative agreement PHY-0757058. Advanced LIGO
225 was built under award PHY-0823459. This document has been assigned LIGO Laboratory
226 document number LIGO-P1500278. The University of Washington, Seattle participation was
227 supported by funding from NSF under award PHY – 1306613. The authors are grateful for useful
228 comments and suggestions by Ryan DeRosa.

229 REFERENCES

230 Aasi, J., B. P. Abbott, R. Abbott, T. Abbott, M. R. Abernathy, K. Ackley, C. Adams, T. Adams,
231 P. Adesso, R. X. Adhikari *et. al.*(2015). Advanced LIGO, *Class. Quantum Grav.* **32** 074001.

232

233 Arp, T. B., C. A. Hagedorn, S. Schlamminger, and J. H. Gundlach (2013). A reference-beam
234 autocollimator with nanoradian sensitivity from mHz to kHz and dynamic range of 10^7 . *Rev. Sci.*
235 *Instrum.* **84**, 095007.

236

237 Dergachev, V., R. DeSalvo, M. Asadoor, A. Bhawal, P. Gong, C. Kim, A. Lottarini, Y.
238 Minenkov, C. Murphy, A. O'Toole, et al. (2014). A high precision, compact electromechanical
239 ground rotation sensor. *Rev. Sci. Instrum.* **85**, no. 5, 054502, doi: [10.1063/1.4875375](https://doi.org/10.1063/1.4875375).

240

241 W. Z. Korth, A. Heptonstall, E. D. Hall, K. Arai, E. K. Gustafson, and R. X. Adhikari (2016).
242 Passive, free-space laser gyroscope, *Class. Quantum Grav.* **33**, 035004.

243

244 Lantz, B., R. Schofield, B. O'Reilly, D. E. Clark, and D. DeBra (2009). Review: Requirements
245 for a ground rotation sensor to improve Advanced LIGO. *Bull. Seismol. Soc. Am.* **99**, no. 2B,
246 980–989.

247

248 Lee, W. K., M. Celebi, M. I. Todorovska, and H. Igel, (2009). Introduction to the special issue on
249 rotational seismology and engineering applications. *Bull. Seismol. Soc. Am.* **99**, no. 2B, 945–957.

250

251 Matichard, F. and M. Evans (2015). Review: Tilt-Free Low Noise Seismometry. *Bull. Seismol.*
252 *Soc. Am.* **105**, no. 2A, 497–510.

253

254 Matichard, F., M. Evans, R. Mittleman, M. McInnis, S. Biscans, K.L. Dooley, H. Sohler, A. Lauriero, H.
255 Paris, J. Koch *et al.* (2016), Modeling and Experiment of the Suspended Seismometer Concept for
256 Attenuating the Contribution of Tilt Motion in Horizontal Measurements. *Rev. Sci. Instrum.* **87**,
257 no. 6, 065002.

258

259 Matichard, F., B. Lantz, R. Mittleman, K. Mason, J. Kissel, B. Abbott, S. Biscans, J. McIver, R.
260 Abbott, S. Abbott, *et al.* (2015). Seismic isolation of Advanced LIGO: Review of strategy,
261 instrumentation and performance, *Class. Quantum Grav.* **32**, 185003.

262

263 O'Toole, A., F. E. Pena Arellano, A. V. Rodionov, M. Shaner, E. Sobacchi, V. Dergachev, R.
264 DeSalvo, M. Asadoor, A. Bhawal, P. Gong, *et al.* (2014). Design and Initial characterization of a
265 compact ultra-high vacuum compatible low frequency tilt accelerometer. *Rev. Sci. Instrum.* **85**,
266 075003, doi: [10.1063/1.4890285](https://doi.org/10.1063/1.4890285).

267

268 Robertson, N. A., R. W. Drever, I. Kerr, and J. Hough (1982). Passive and active seismic
269 isolation for gravitational radiation detectors and other instruments, *J. Phys. Sci. Instrum.* **15**, no.
270 10, 1101

271

272 Rodgers, P. W. (1968). The response of the horizontal pendulum seismometer to Rayleigh and
273 Love waves, tilt, and free oscillations of the Earth. *Bull. Seismol. Soc. Am.* **58**, no. 5, 1385–1406.

274

275 Schreiber, K. U., and J. P. R. Wells (2013). Invited review article: Large ring lasers for rotation
276 sensing. *Rev. Sci. Instrum.* **84**, no. 4, 041101.

277

278 Speake, C. C., and D. B. Newell (1990). *Rev. Sci. Instrum.* **61**, 1500.

279

280 Venkateswara, K., C. A. Hagedorn, M. D. Turner, T. Arp, and J. H. Gundlach (2014). A high
281 precision mechanical absolute-rotation sensor. *Rev. Sci. Instrum.* **85**, no. 1, 015005, doi:
282 [10.1063/1.4862816](https://doi.org/10.1063/1.4862816).

283

284 Winterflood, J., Z. B. Zhou, L. Ju, and D. G. Blair (2000), Tilt suppression for ultra-low residual
285 motion vibration isolation in gravitational wave detection, *Phys. Lett. A* **277**, no. 3, 143–155.

286

287 **Full mailing address of each author**

288 Krishna Venkateswara (kvenk@uw.edu)

289 Charlie Hagedorn (cah49@uw.edu)

290 Jens Gundlach (jens@phys.washington.edu)

291 180, North Physics Lab bldg.,

292 CENPA, Box 354290

293 Seattle, WA 98195 USA

294

295 Jeff Kissel (jkissel@ligo.mit.edu)

296 Jim Warner (warner_j@ligo-wa.caltech.edu)

297 Hugh Radkins (radkins_h@ligo-wa.caltech.edu)

298 Thomas Shaffer (Shaffer_t@ligo-wa.caltech.edu)

299 LIGO Hanford Observatory

300 127124 N Route 10,

301 Richland WA 99354 USA

302

303 Brian Lantz (blantz@stanford.edu)

304

305 Richard Mittleman (richard@ligo.mit.edu)

306 Fabrice Matichard (fabrice@ligo.mit.edu)

307 LIGO Project MIT

308 MIT NW22-295

309 185 Albany street

310 Cambridge MA 02139 USA

311

312 Robert Schofield (rmssrmss@gmail.com)

313

314 List of Figure Captions

315 Figure 1: Schematic of the beam-balance. θ_p is the angle of the ground w.r.t. a local inertial
316 frame, θ_i is the angle of the beam-balance w.r.t. the inertial frame and $\theta_a = \theta_i - \theta_p$ is the
317 angle measured by the autocollimator.

318 Figure 2: BRS raw angle measurement during high-winds. The solid curve is the angle of the
319 beam-balance as measured by the autocollimator. The dashed curve is a measure of the
320 autocollimator self-noise.

321 Figure 3: Wind-speed data from May 16 2015.

322 Figure 4: Ground tilt computation using BRS and T240. The ground tilt measured with BRS
323 (solid) is corrected for finite acceleration coupling using the T240 (dashed) yielding the dotted
324 curve. Also shown is the autocollimator noise contribution (dash-dot).

325 Figure 5: Tilt-subtraction in T240 acceleration data taken under windy conditions on May 16 2015. The
326 tilt-subtracted residual acceleration is significantly smaller than the measured acceleration between 10-
327 100 mHz.

328 Figure 6: Tilt to Translation transfer function. This plot shows the relation between the
329 translation measured by the seismometer and the tilt measured by BRS. It has the expected g/ω^2
330 relation at low-frequencies but also shows a linear dependence at higher frequencies.

331 Figure 7: Coherence between T240, BRS and acceleration residuals, and the expected and
332 measured subtraction factors.

333 Figure 8: ASD and coherence of data under windy conditions on October 11 2014. The primary
334 micro-seismic peak is visible after tilt-subtraction and is a consistent height over time.

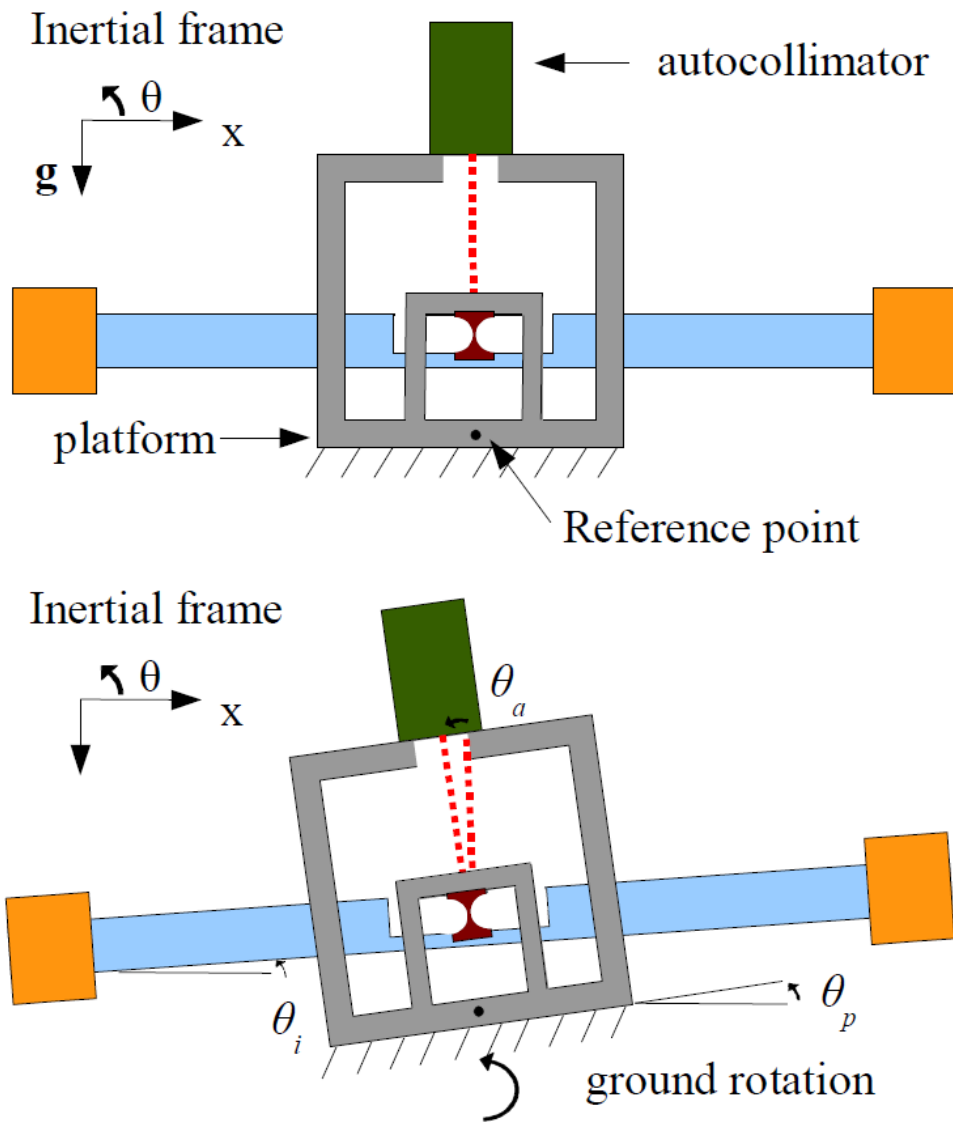
335 Figure 9: Wind speed data from October 11 2014.

336 Figure 10: ASD and coherence of data during low wind-speeds on May 14 2015.

337 Figure 11: Wind-speed data from May 14 2015

338 Figure 12: BRS readout noise contribution compared to the Lantz et. al. (2009) requirement.
339 Also shown are the tilt-subtracted residual accelerations during low-wind and high-wind periods,
340 converted to tilt units by dividing by g .

341 **Figures**

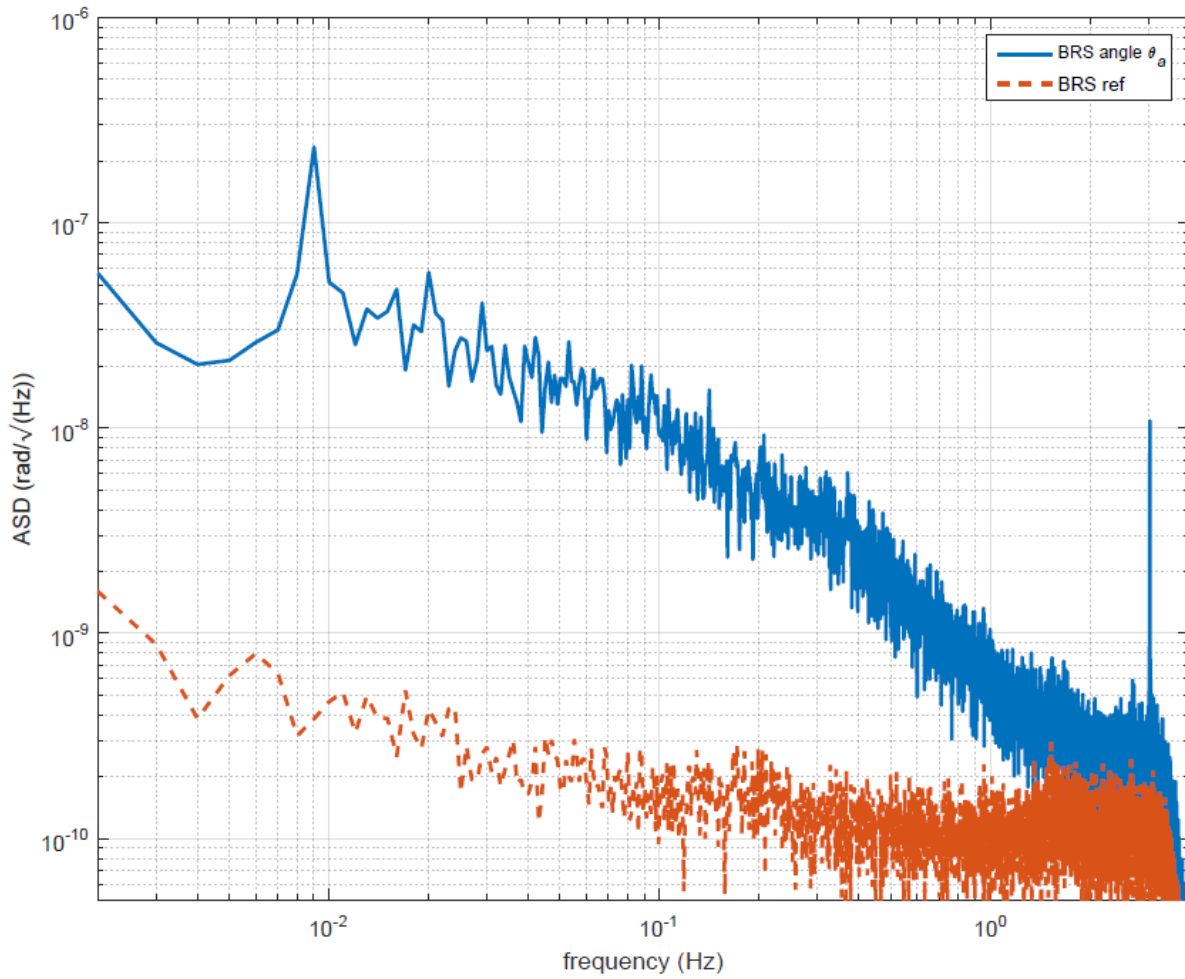


342

343 **Figure 1: Schematic of the beam-balance. θ_p is the angle of the ground w.r.t. a local inertial**

344 **frame, θ_i is the angle of the beam-balance w.r.t. the inertial frame and $\theta_a = \theta_i - \theta_p$ is the**

345 **angle measured by the autocollimator.**

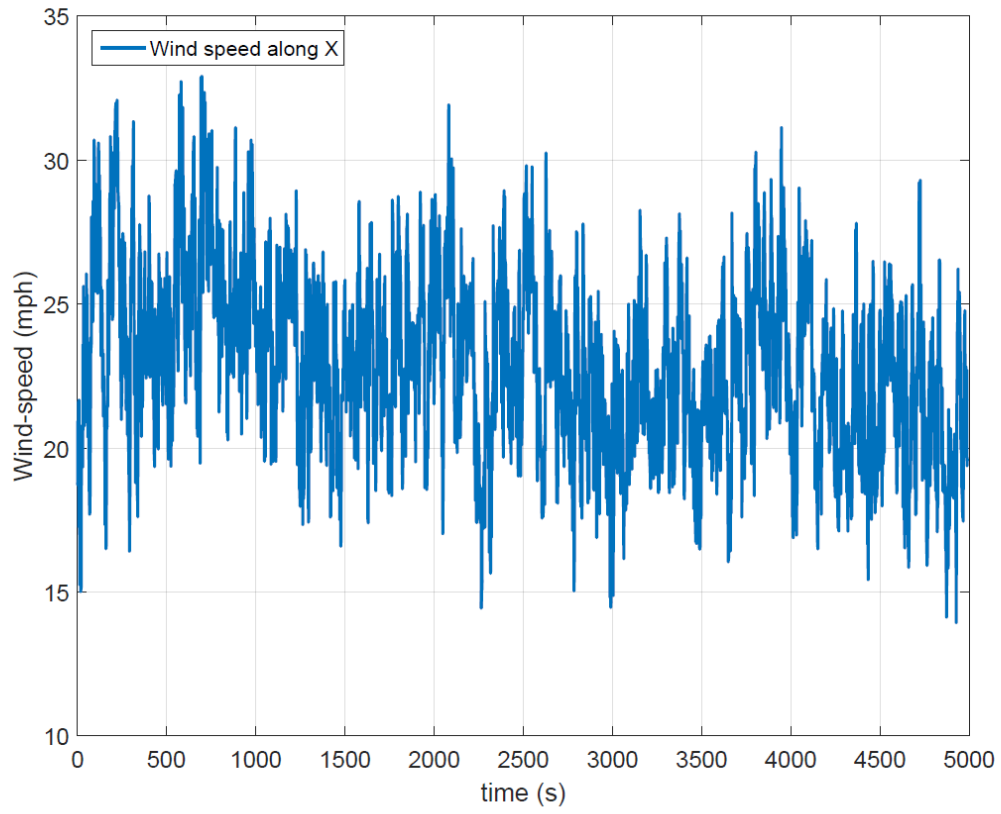


346

347 **Figure 2: BRS raw angle measurement during high-winds. The solid curve is the angle of**

348 **the beam-balance as measured by the autocollimator. The dashed curve is a measure of the**

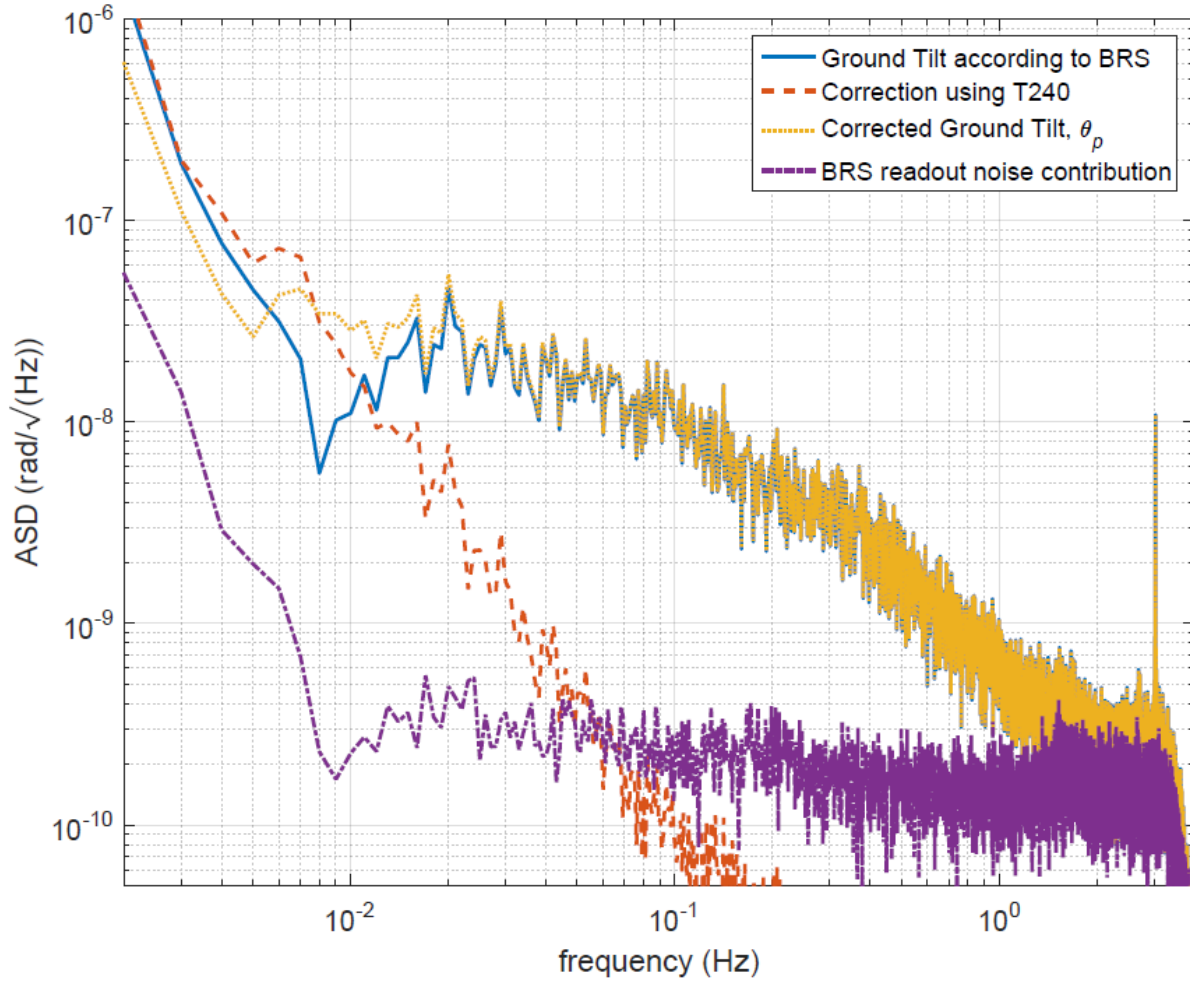
349 **autocollimator self-noise.**



350

351

Figure 3: Wind-speed data from May 16 2015.



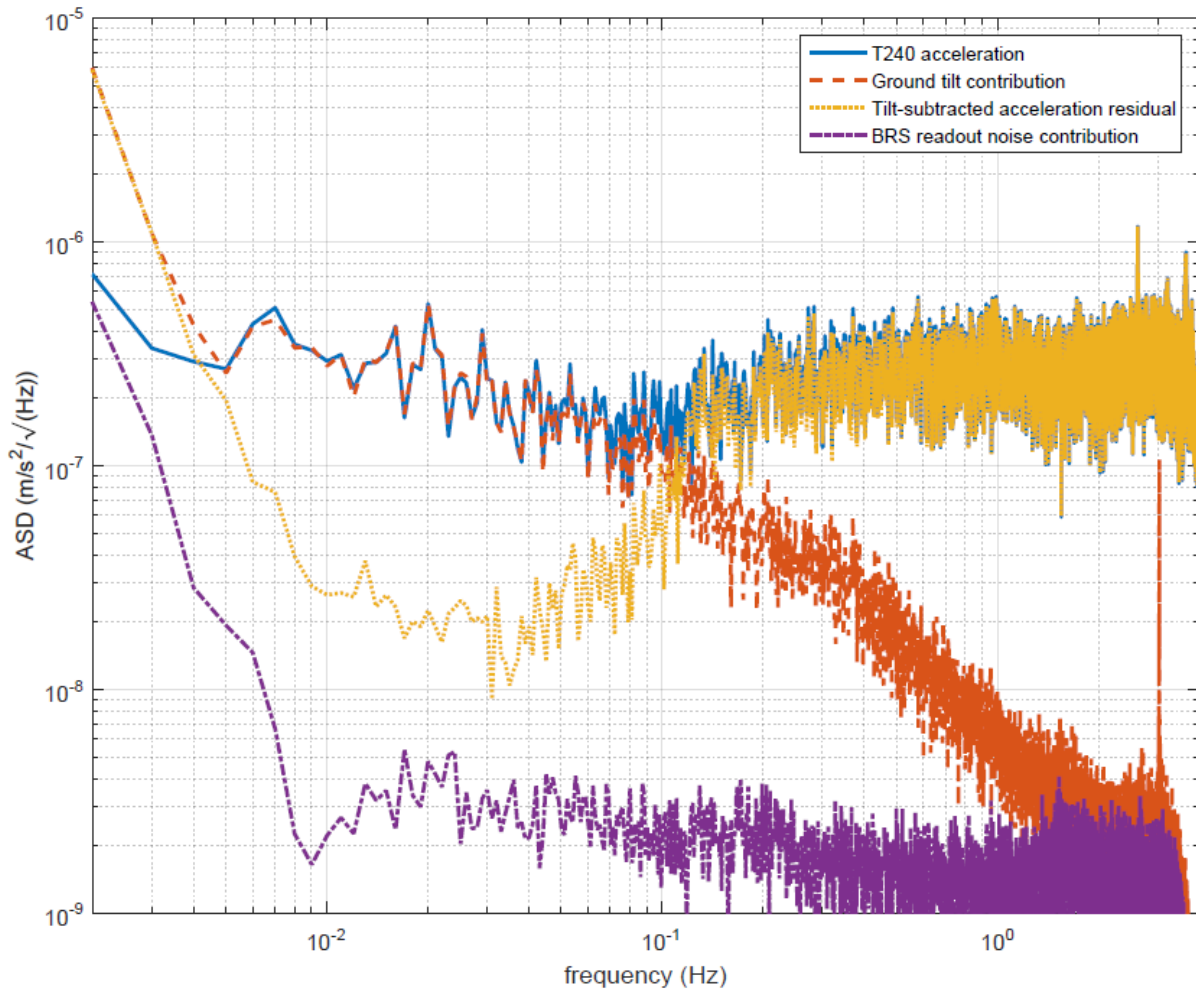
352

353

354

355

Figure 4: Ground tilt computation using BRS and T240. The ground tilt measured with BRS (solid) is corrected for finite acceleration coupling using the T240 (dashed) yielding the dotted curve. Also shown is the autocollimator noise contribution (dash-dot).

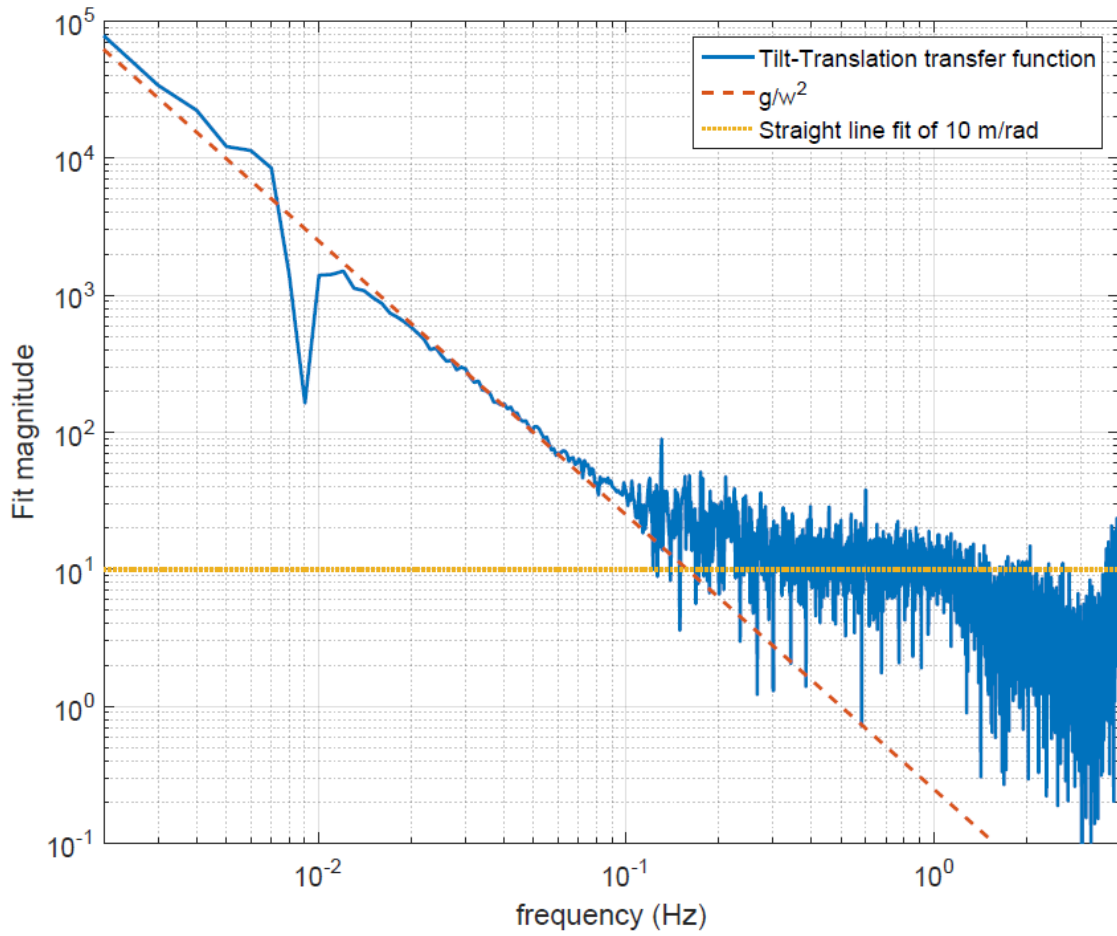


356

357 **Figure 5: Tilt-subtraction in T240 acceleration data taken under windy conditions on May 16 2015.**

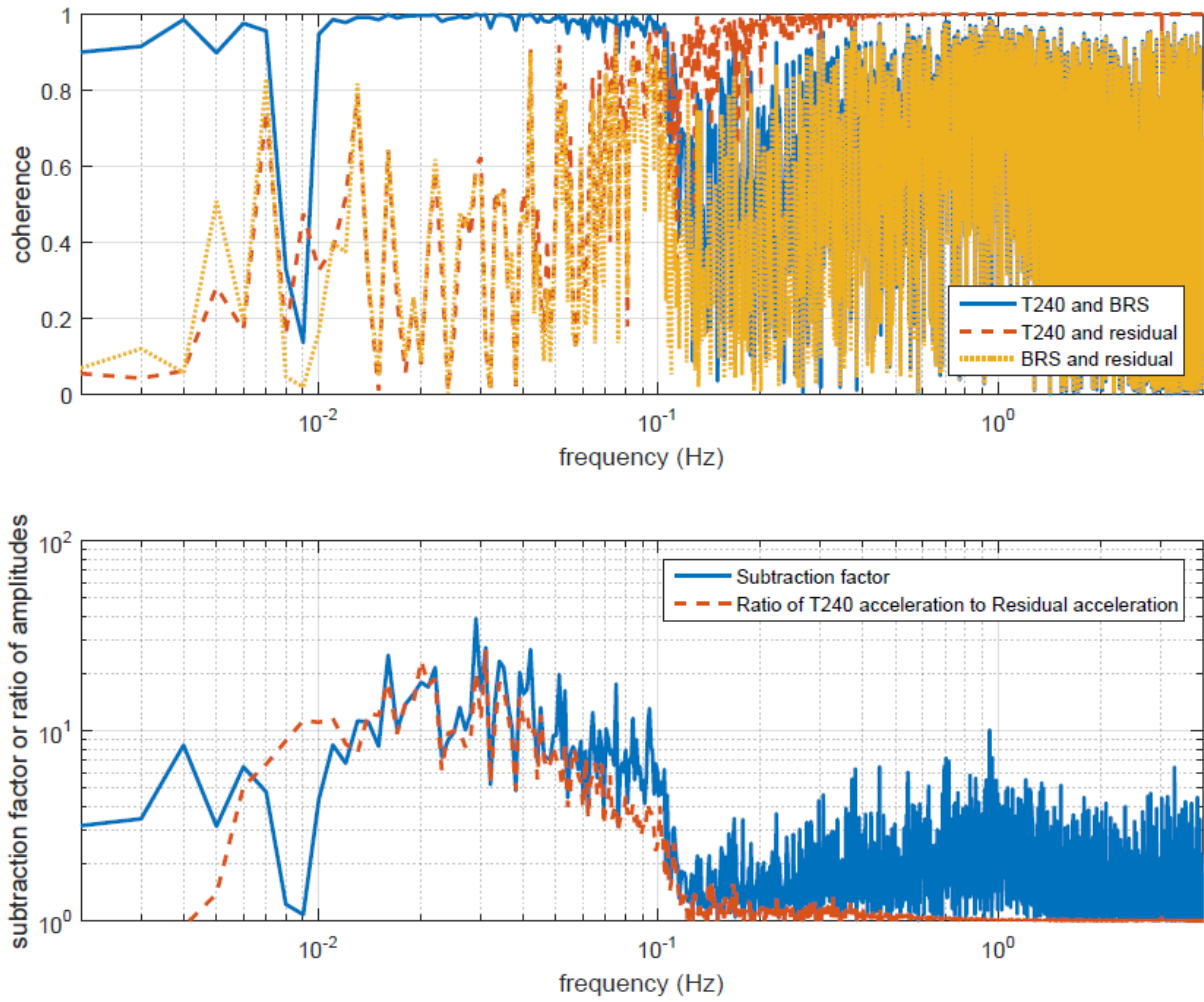
358 **The tilt-subtracted residual acceleration is significantly smaller than the measured acceleration**

359 **between 10-100 mHz.**



360

361 **Figure 6: Tilt to Translation transfer function.** This plot shows the relation between the
362 translation measured by the seismometer and the tilt measured by BRS. It has the expected
363 g/ω^2 relation at low-frequencies but also shows a linear dependence at higher frequencies.

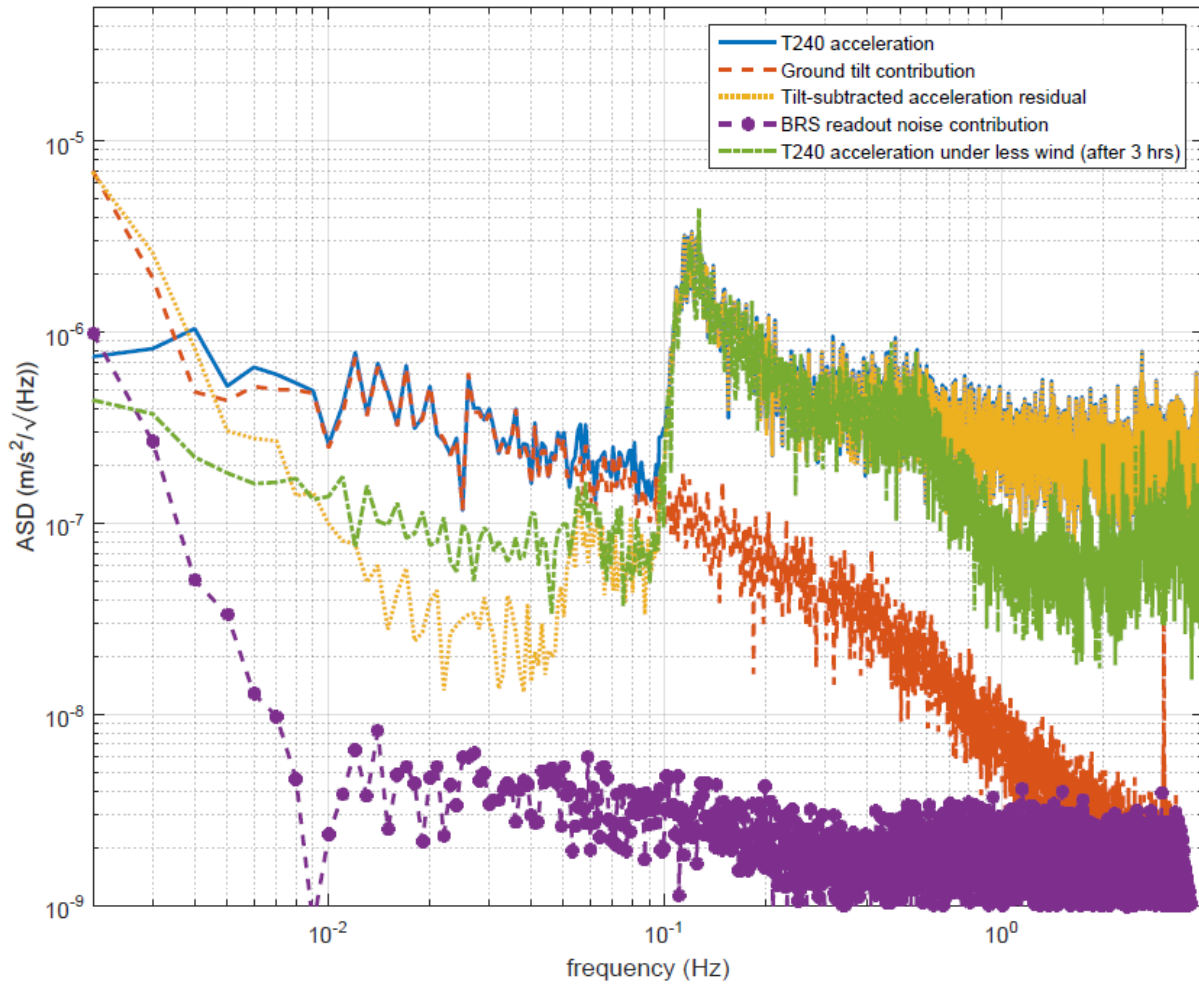


364

365 **Figure 7: Coherence between T240, BRS and acceleration residuals, and the expected and**

366

measured subtraction factors.



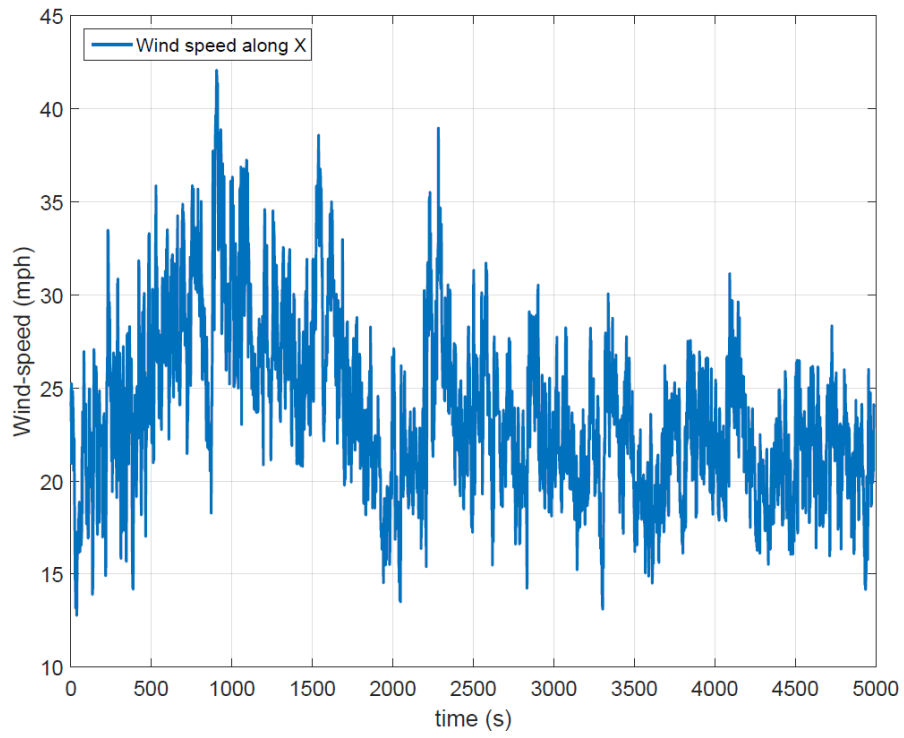
367

368

369

370

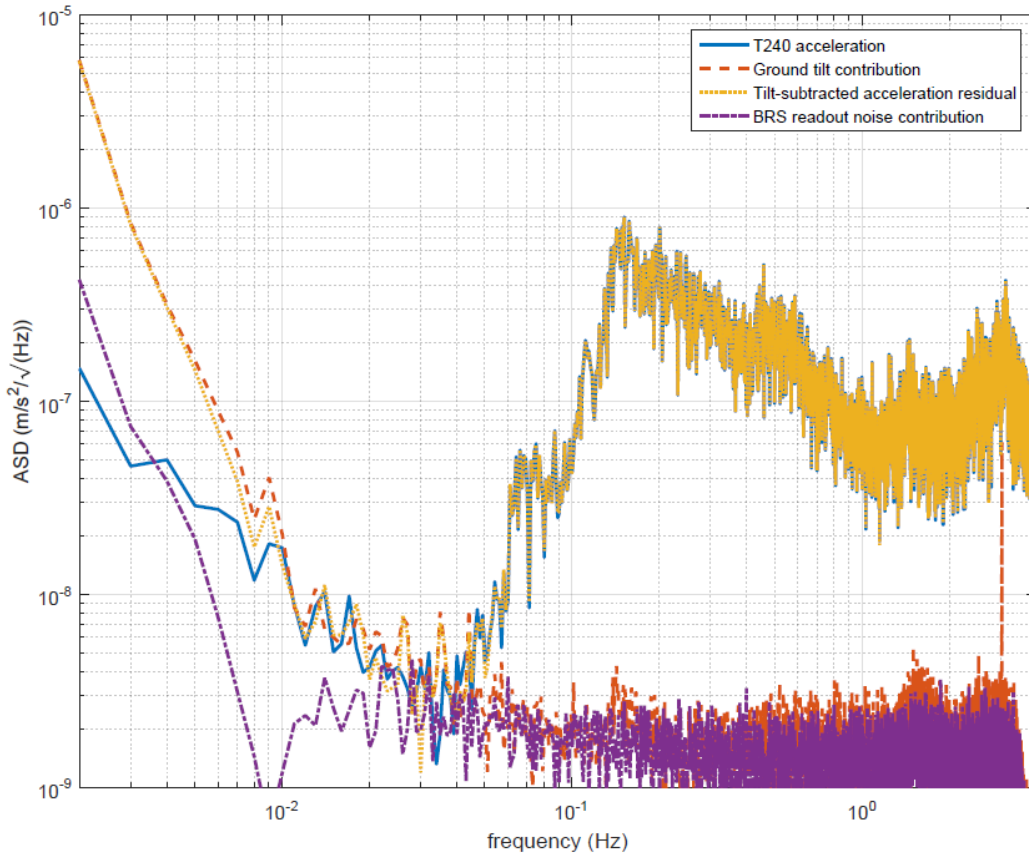
Figure 8: ASD and coherence of data under windy conditions on October 11 2014. The primary micro-seismic peak is visible after tilt-subtraction and is a consistent height over time.



371

372

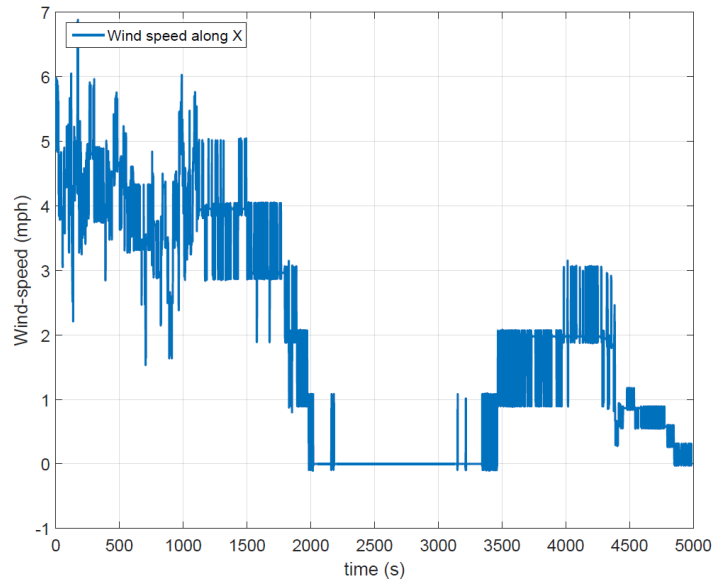
Figure 9: Wind speed data from October 11 2014.



373

374

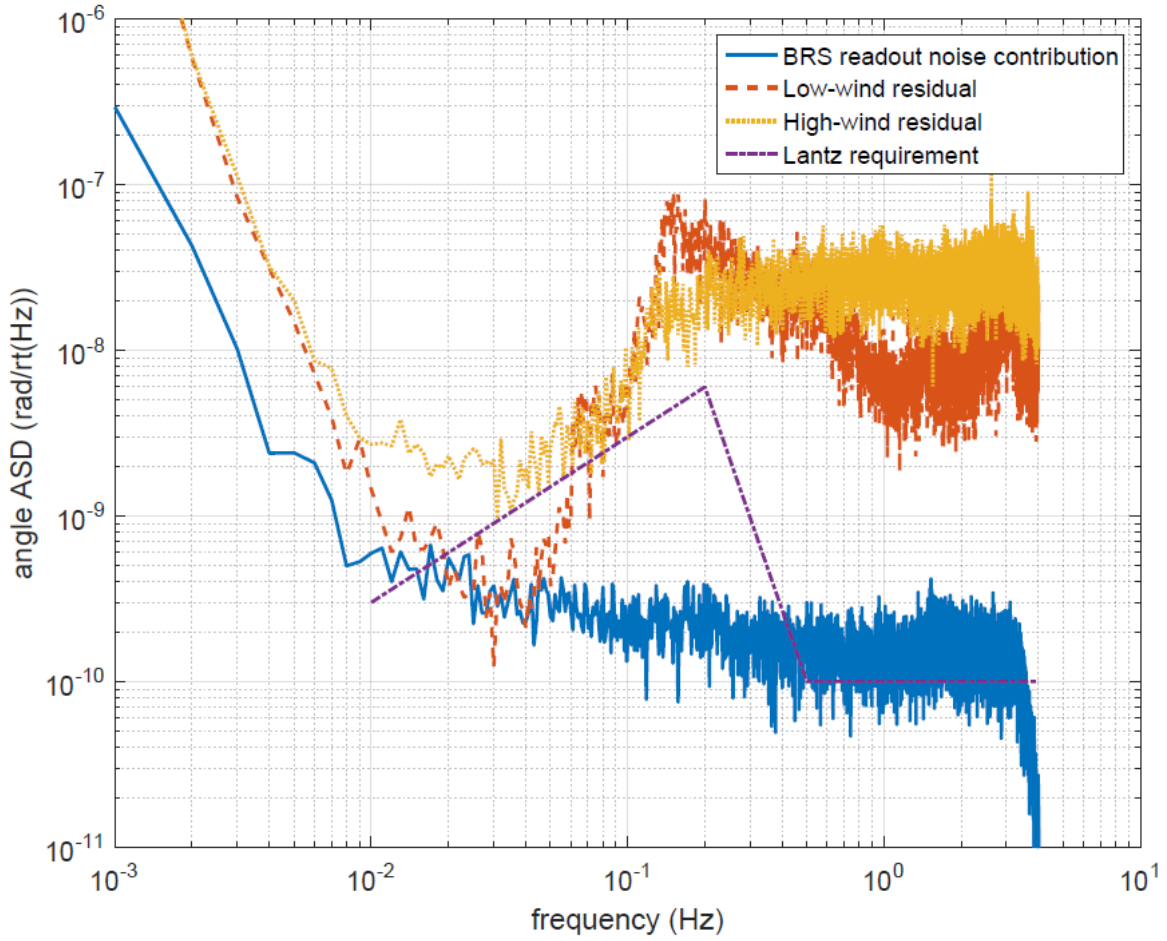
Figure 10: ASD and coherence of data during low wind-speeds on May 14 2015.



375

376

Figure 11: Wind-speed data from May 14 2015.



377

378 **Figure 12: BRS readout noise contribution compared to the Lantz et. al. (2009) requirement. Also**
 379 **shown are the tilt-subtracted residual accelerations during low-wind and high-wind periods,**
 380 **converted to tilt units by dividing by g .**

381

382 Appendix A: Equations of motion and tilt-subtraction

383 The torque on the beam-balance, as measured in the lab-frame can be expressed as

$$\tau = I\ddot{\theta}_a + \kappa(1 + i\varphi)\theta_a \quad (\text{A1})$$

384 where I is the moment of inertia and κ is the flexure torsional stiffness and φ is the flexure's
 385 intrinsic loss factor. It can be shown (Venkateswara *et al.* (2014)) that the measured torque is

$$\tau = \tau_{ext.} - I\ddot{\theta}_p - Mda_x \quad (\text{A2})$$

386 where M is the total mass of the balance, d is the separation between the center of mass (COM)
 387 and the suspension point/pivot ($d > 0$ if COM is below the pivot) and $a_x = \ddot{x} + g\theta_p$ is the
 388 horizontal acceleration at the pivot. Ignoring small corrections due to the location difference
 389 between the T240 and BRS, we assume that a_x is equal to the acceleration measured by the
 390 T240. $\tau_{ext.}$ is the sum of all external torques on the balance. This can include terms like
 391 Brownian-motion torques, torques from gravity gradients etc., which are usually quite small. The
 392 last two terms in the above equation can also be interpreted as the pseudo forces due to the non-
 393 inertial lab frame. This relation can be rewritten in frequency space as

$$-I\theta_a\omega^2 + I\theta_a\omega_0^2(1 + i\varphi) = \tau_{ext.} + I\theta_p\omega^2 + Md(g\theta_p - x\omega^2) \quad (\text{A3})$$

394 where ω_0 is the resonance frequency of the beam-balance and we have retained the same
 395 symbols for the Fourier transforms of the original variables for convenience. Setting ground
 396 displacement to 0, the tilt-response of BRS in frequency-space is

$$\frac{\text{Measured angle}}{\text{Input Angle}} = \frac{\theta_a}{\theta_p} = \frac{\omega^2 - \omega_g^2}{\omega^2 - \omega_0^2(1 + i\varphi)} \quad (\text{A4})$$

397 where $\omega_g = \sqrt{\frac{Mgd}{I}}$. The response is flat and unity at frequencies well above the resonance, goes
 398 to zero at ω_g and goes to a constant value at low frequencies. The high-frequency response
 399 ($\omega \gg \omega_0$) is due to the inertia of the balance, while the response at low frequencies ($\omega \ll \omega_0$)
 400 comes from its acceleration sensitivity (due to finite 'd'). The zero in the response, ω_g , is the
 401 frequency at which these two effects are equal and opposite.

402 The response to horizontal acceleration is given by

$$\frac{\text{Measured Angle}}{\text{Input acceleration}} = \frac{Md}{I} \frac{1}{\omega^2 - \omega_0^2(1 + i\varphi)} \quad (\text{A5})$$

403 Based on the above, one would like to design the balance such that ‘ d ’ is as small as possible in
 404 order to minimize acceleration coupling. In practice, it can be adjusted by measuring the driven-
 405 transfer function of the instrument and adding trim weights to the balance to make it small. For
 406 the BRS, d was about (33 +/- 5) micrometers.

407 To separate the horizontal acceleration measured by a seismometer into displacement and
 408 rotation components, we can use the fact that the seismometer measures the net horizontal
 409 acceleration, a_x , and express the ground rotation in terms of the BRS measurement, θ_a , and a_x .
 410 Using eq. (**Error! Reference source not found.**), the ground rotation w.r.t. an inertial frame can
 411 be expressed as

$$\theta_p = -\frac{\omega^2 - \omega_0^2(1 + i\varphi)}{\omega^2} \theta_a + \frac{Md}{I\omega^2} a_x \quad (\text{A6})$$

412 This ‘inertial’-ground rotation (times g) can then be subtracted from a seismometer’s
 413 acceleration, thus separating displacement and rotation.

414 Appendix B: Influence of earth’s rotation

415 In estimating the magnitude of the effect of earth’s rotation on the balance, it is useful to
 416 compare the torques on the balance produced by these effects to that produced by tilt. The torque
 417 from a ground rotation of $\theta_s \sim 10 \text{ nrad}/\sqrt{(\text{Hz})}$ is

$$\tau_s = I\theta_s\omega^2 \quad (\text{B1})$$

418 where ω is the frequency of the signal and I is the moment of inertia of BRS. Since the angular
 419 effects of torque are inversely proportional to frequency squared, we will examine them at 10
 420 mHz where they will have the largest effect. At 10 mHz, the torque from the ground rotation is \sim
 421 10^{-11} N-m/ $\sqrt{(\text{Hz})}$.

422 Torques due to earth's rotation would arise if the balance moved in the horizontal plane relative
 423 to an inertial frame. Let's call this angular motion as θ_h . In general, we expect θ_h to be smaller
 424 than θ_s as torsional motion of the ground is harder to produce than tilt. Then the torque due to
 425 the centrifugal force from earth's rotation is

$$\tau_{cen.} = I(\Omega_E)^2 \theta_h \cos(\varphi) \sin(\varphi) \cos(\alpha) \quad (\text{B2})$$

426 where Ω_E is the angular frequency of earth's rotation, φ is the latitude of the BRS location and α
 427 is the angle BRS makes with the East-West direction. Assuming worst-case orientation, this
 428 gives $\tau_{cen.} \approx 10^{-17}$ N-m/ $\sqrt{(\text{Hz})}$ for $\theta_h \sim 10$ nrad/rt(Hz). This is negligibly small compared to the
 429 torque from ground rotation.

430 The maximum torque due to the Coriolis force is

$$\tau_{cor.} = I\Omega_E \omega \theta_h \cos(\varphi) \sin(\alpha) \quad (\text{B3})$$

431 At 10 mHz, this gives $\tau_{cor.} \approx 10^{-14}$ N-m/ $\sqrt{(\text{Hz})}$ for $\theta_h \sim 10$ nrad/rt(Hz). This is more
 432 significant, but still three orders of magnitude smaller than the signal torque of interest. In angle
 433 units, this would correspond to a tilt noise of ~ 0.01 nrad/ $\sqrt{(\text{Hz})}$, which is more than an order of
 434 magnitude below the requirement for the sensor.